



GOALS-JWST: Mid-infrared Spectroscopy of the Nucleus of NGC 7469

Downloaded from: <https://research.chalmers.se>, 2025-05-17 09:34 UTC

Citation for the original published paper (version of record):

Armus, L., Lai, T., Vivian, U. et al (2023). GOALS-JWST: Mid-infrared Spectroscopy of the Nucleus of NGC 7469. *Astrophysical Journal Letters*, 942(2).

<http://dx.doi.org/10.3847/2041-8213/acac66>

N.B. When citing this work, cite the original published paper.



GOALS-JWST: Mid-infrared Spectroscopy of the Nucleus of NGC 7469

L. Armus¹, T. Lai¹, V. U², K. L. Larson³, T. Diaz-Santos^{4,5}, A. S. Evans^{6,7}, M. A. Malkan⁸, J. Rich⁹, A. M. Medling^{10,11}, D. R. Law¹², H. Inami¹³, F. Muller-Sanchez¹⁴, V. Charmandaris^{4,5,15}, P. van der Werf¹⁶, S. Stierwalt¹⁷, S. Linden¹⁸, G. C. Privon^{6,19}, L. Barcos-Muñoz⁷, C. Hayward²⁰, Y. Song^{6,7}, P. Appleton¹, S. Aalto²¹, T. Bohn¹³, T. Böker²², M. J. I. Brown²³, L. Finnerty⁸, J. Howell¹, K. Iwasawa^{24,25}, F. Kemper^{26,27,28}, J. Marshall²⁹, J. M. Mazzarella¹, J. McKinney³⁰, E. J. Murphy⁶, D. Sanders³¹, and J. Surace¹

¹IPAC, California Institute of Technology, 1200 East California Boulevard, Pasadena, CA 91125, USA; lee@ipac.caltech.edu

²Department of Physics and Astronomy, 4129 Frederick Reines Hall, University of California, Irvine, CA 92697, USA

³AURA for the European Space Agency (ESA), Space Telescope Science Institute, 3700 San Martin Drive, Baltimore, MD 21218, USA

⁴Institute of Astrophysics, Foundation for Research and Technology-Hellas (FORTH), Heraklion, 70013, Greece

⁵School of Sciences, European University Cyprus, Diogenes Street, Engomi, 1516 Nicosia, Cyprus

⁶National Radio Astronomy Observatory, 520 Edgemont Road, Charlottesville, VA 22903, USA

⁷Department of Astronomy, University of Virginia, 530 McCormick Road, Charlottesville, VA 22903, USA

⁸Department of Physics & Astronomy, 430 Portola Plaza, University of California, Los Angeles, CA 90095, USA

⁹The Observatories of the Carnegie Institution for Science, 813 Santa Barbara Street, Pasadena, CA 91101, USA

¹⁰Department of Physics & Astronomy and Ritter Astrophysical Research Center, University of Toledo, Toledo, OH 43606, USA

¹¹ARC Centre of Excellence for All Sky Astrophysics in 3 Dimensions (ASTRO 3D); Australia

¹²Space Telescope Science Institute, 3700 San Martin Drive, Baltimore, MD 21218, USA

¹³Hiroshima Astrophysical Science Center, Hiroshima University, 1-3-1 Kagamiyama, Higashi-Hiroshima, Hiroshima 739-8526, Japan

¹⁴Department of Physics and Materials Science, The University of Memphis, 3720 Alumni Avenue, Memphis, TN 38152, USA

¹⁵Department of Physics, University of Crete, Heraklion, 71003, Greece

¹⁶Leiden Observatory, Leiden University, PO Box 9513, 2300 RA Leiden, The Netherlands

¹⁷Physics Department, Occidental College, 1600 Campus Road, Los Angeles, CA 90041, USA

¹⁸Department of Astronomy, University of Massachusetts at Amherst, Amherst, MA 01003, USA

¹⁹Department of Astronomy, University of Florida, PO Box 112055, Gainesville, FL 32611, USA

²⁰Center for Computational Astrophysics, Flatiron Institute, 162 Fifth Avenue, New York, NY 10010, USA

²¹Department of Space, Earth and Environment, Chalmers University of Technology, SE-412 96 Gothenburg, Sweden

²²European Space Agency, Space Telescope Science Institute, Baltimore, MD 21218, USA

²³School of Physics and Astronomy, Monash University, Clayton, VIC 3800, Australia

²⁴Institut de Ciències del Cosmos (ICCUB), Universitat de Barcelona (IEEC-UB), Martí i Franquès, 1, E-08028 Barcelona, Spain

²⁵ICREA, Pg. Lluís Companys 23, E-08010 Barcelona, Spain

²⁶Institut de Ciències de l'Espai (ICE, CSIC), Can Magrans, s/n, E-08193 Bellaterra, Barcelona, Spain

²⁷ICREA, Pg. Lluís Companys 23, Barcelona, Spain

²⁸Institut d'Estudis Espacials de Catalunya (IEEC), E-08034 Barcelona, Spain

²⁹Glendale Community College, 1500 North Verdugo Road, Glendale, CA 91208, USA

³⁰Department of Astronomy, University of Massachusetts, Amherst, MA 01003, USA

³¹Institute for Astronomy, University of Hawaii, 2680 Woodlawn Drive, Honolulu, HI 96822, USA

Received 2022 September 26; revised 2022 December 9; accepted 2022 December 12; published 2023 January 13

Abstract

We present mid-infrared spectroscopic observations of the nucleus of the nearby Seyfert galaxy NGC 7469 taken with the MIRI instrument on the James Webb Space Telescope (JWST) as part of Directors Discretionary Time Early Release Science program 1328. The high-resolution nuclear spectrum contains 19 emission lines covering a wide range of ionization. The high-ionization lines show broad, blueshifted emission reaching velocities up to 1700 km s⁻¹ and FWHM ranging from ~500 to 1100 km s⁻¹. The width of the broad emission and the broad-to-narrow line flux ratios correlate with ionization potential. The results suggest a decelerating, stratified, AGN-driven outflow emerging from the nucleus. The estimated mass outflow rate is 1–2 orders of magnitude larger than the current black hole accretion rate needed to power the AGN. Eight pure rotational H₂ emission lines are detected with intrinsic widths ranging from FWHM ~125 to 330 km s⁻¹. We estimate a total mass of warm H₂ gas of ~1.2 × 10⁷ M_⊙ in the central 100 pc. The PAH features are extremely weak in the nuclear spectrum, but a 6.2 μm PAH feature with an equivalent width of ~0.07 μm and a flux of 2.7 × 10⁻¹⁷ W m⁻² is detected. The spectrum is steeply rising in the mid-infrared, with a silicate strength of ~0.02, significantly smaller than seen in most PG QSOs but comparable to other Seyfert 1s. These early MIRI mid-infrared IFU data highlight the power of JWST to probe the multiphase interstellar media surrounding actively accreting supermassive black holes.

Unified Astronomy Thesaurus concepts: Active galaxies (17); Starburst galaxies (1570); Infrared galaxies (790)

1. Introduction

Luminous infrared galaxies (LIRGs), with thermal IR [8–1000 μm] dust emission in excess of 10¹¹ L_⊙, are ideal laboratories for studying star formation and black hole growth in the local universe. The bolometric luminosity of most LIRGs is dominated by massive bursts of star formation but also

shows a wide range of contributions from active galactic nuclei (AGN), which become increasingly important at the highest luminosities (Petric et al. 2011; Stierwalt et al. 2013, 2014). Multiwavelength observations have shown that local LIRGs are a mixture of single disk galaxies, interacting systems, and advanced mergers (Kim et al. 2013; Stierwalt et al. 2013; Larson et al. 2016).

Our understanding of the energetics and evolutionary states of LIRGs at low and high redshifts was greatly expanded through studies with the Infrared Spectrograph (IRS; see Houck et al. 2004) on the Spitzer Space Telescope (see Armus et al. 2020, for a summary). While Spitzer was extremely efficient and capable of deep, as well as large-area, photometric and spectroscopic surveys, it was ultimately limited in sensitivity and spatial resolution by its modest 0.85 m primary mirror. With the successful launch and commissioning of the James Webb Space Telescope (JWST) and its 1–2 orders of magnitude gain in both sensitivity and spatial and spectral resolution over Spitzer, we are now poised to greatly extend our understanding of dusty star-forming regions, nascent AGN, galactic outflows, and all variety of active galaxies over an extremely large stretch of cosmic time. To highlight the power of JWST to explore the inner regions of nearby LIRGs, we have undertaken a Director’s Discretionary Time Early Release Science (ERS) program (1328; PIs: L. Armus, A. S. Evans) to obtain near and mid-infrared images and spectra of four LIRGs drawn from the Great Observatories All-Sky LIRG Survey (GOALS; Armus et al. 2009). GOALS uses multiwavelength observations from the ground and space to understand the physical conditions in over 200 low-redshift ($z < 0.09$) LIRGs selected from the Revised IRAS Bright Galaxy Sample (Sanders et al. 2003). This paper highlights some of the first results from ERS program 1328, “A JWST Study of the Starburst-AGN Connection in Merging Luminous Infrared Galaxies.”

Object NGC 7469 (IRAS 23007+0836; UGC 12332) contains a Seyfert 1.5 nucleus surrounded by a bright, circumnuclear ring of star formation with a radius of $1''.8$ (580 pc). The total infrared luminosity of NGC 7469 is $4.5 \times 10^{11} L_{\odot}$. It is a nearly face-on spiral, about 26 kpc away in projection from an inclined companion galaxy (IC 4283) with a highly disturbed morphology. It has a supermassive black hole (SMBH) mass of $\sim 10^7 M_{\odot}$, measured through reverberation mapping (Peterson et al. 2004). The starburst ring is visible at multiple wavelengths, with a large number of star-forming regions having a bimodal age distribution (Díaz-Santos et al. 2007). There is evidence for a highly ionized, outflowing wind on small and large scales (Muller-Sanchez et al. 2011; U et al. 2019; Arav et al. 2020; Robleto-Orus et al. 2021). The mid-infrared Spitzer spectrum of NGC 7469 shows a mix of strong polycyclic aromatic hydrocarbon (PAH) emission features, high-ionization lines, and warm molecular gas indicative of a composite source powered by an active nucleus and a starburst (Inami et al. 2013; Stierwalt et al. 2014). High-resolution observations of CO(1–0), CO(2–1), and [C I] in the inner ~ 2 kpc region with the Atacama Large Millimeter/submillimeter Array (ALMA) show largely rotational kinematics and a large mass of molecular gas (Izumi et al. 2020; Nguyen et al. 2021). With a central AGN, a circumnuclear starburst ring, a high-velocity outflow, and a dusty, gas-rich interstellar medium (ISM), NGC 7469 is an

ideal laboratory for studying the coevolution of galaxies and SMBHs at high resolution with JWST.

Here we present JWST integral field spectroscopic observations of the nucleus of NGC 7469 with the Mid-Infrared Instrument (MIRI; Rieke et al. 2015; Labiano et al. 2021). The high spectral–spatial resolution enables us to map the physical properties and kinematics of the atomic and warm molecular gas, as well as the dust on subkiloparsec scales in the mid-infrared for the first time. Specifically, the integral field unit (IFU) data allow us to separately extract and analyze the high signal-to-noise, mid-infrared spectra of the starburst ring, inner ISM, and central AGN. The ring spectra are presented in Lai & Armus (2022). The spectra of the circumnuclear ISM are presented in U et al. (2022). Here we focus on the MIRI spectra of the central active nucleus. Throughout this paper, we adopt $H_0 = 70 \text{ km s}^{-1} \text{ Mpc}^{-1}$, $\Omega_m = 0.30$, and $\Omega_{\text{vac}} = 0.70$. At the distance of NGC 7469, 70.6 Mpc ($z = 0.01627$), $1''$ subtends a projected linear scale of 330 pc.

2. Observations and Data Reduction

Observations of NGC 7469 were taken with MIRI in Medium Resolution Spectroscopy (MRS) mode on 2022 July 3–4 UT. The observations covered the full 4.9–28.8 μm range using the short (A), medium (B), and long (C) subbands in all four channels. The FASTR1 readout pattern was used to optimize the dynamic range in the observations. The total exposure time per subband was 444 s, using 40 groups per integration and a four-point dither pattern. Because NGC 7469 is extended, dedicated background observations with the same observational parameters in all three grating settings were obtained. MIRI imaging observations were taken using three filters, F560W, F770W, and F1500W, using a cycling three-point dither pattern. Data were collected with both the full imaging field of view ($74'' \times 113''$) and the SUB128 subarray mode ($14''.1 \times 14''.1$) to recover a nonsaturated image of the bright nucleus. The total exposure times are 309, 101, and 101 s and 46, 48, and 48 s for the F560W, F770W, and F1500W filters and full and subarray modes, respectively. The MIRI and NIRCам imaging of the starburst ring in NGC 7469 will be presented in Bohn et al. (2022).

Data for the science and background observations were processed with the JWST Science Calibration Pipeline (Bus-house et al. 2022) version 1.6+ in batch mode. The Detector1 pipeline applies detector-level corrections and ramp fitting to the individual exposures. The output rate images were subsequently processed outside the JWST pipeline to flag newly acquired bad pixels and additional cosmic-ray artifacts and remove the vertical stripes and zero-point residuals remaining after the pipeline dark subtraction. These additional corrections broadly follow the steps taken for JWST Early Release Observation (ERO) observations as described by Pontoppidan et al. (2022). The resulting rate files are then processed with the JWST Spec2 pipeline for distortion and wavelength calibration, flux calibration, and other 2D detector-level steps. Stage 3 processing (Spec3) performs background subtraction before combining data from multiple exposures into the final data cubes. Background light is subtracted from the 2D science images using a master background frame generated from our associated background observations. The master background is a 1D median sigma-clipped spectrum calculated over the field of view of the background observations and projected to the entire 2D detector array. Residual fringe

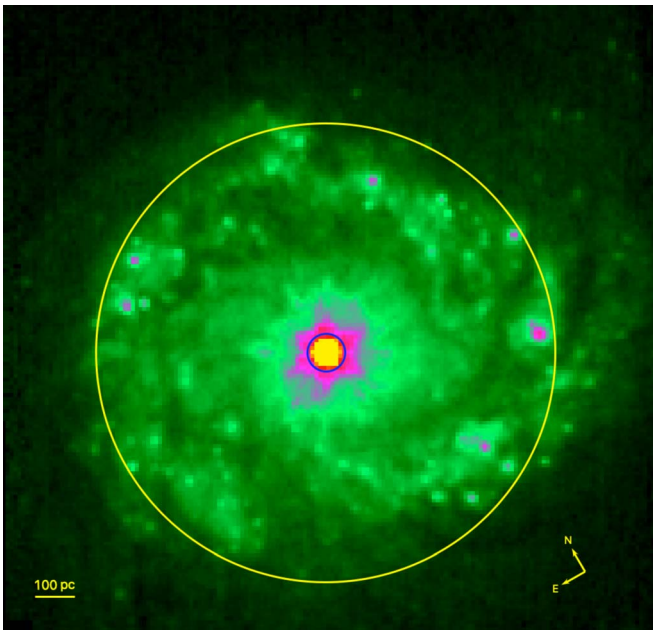


Figure 1. False-color JWST NIRCcam F150W subarray image of the center of NGC 7469. The image, which is $5''.1$ (1.65 kpc) across, shows the bright, central AGN and the surrounding starburst ring, which is resolved into dozens of star-forming knots, interspersed with regions of diffuse emission and dark dust lanes. In the image, two circles are shown that represent the extraction regions for the MIRI total (large yellow circle; $3''.6$ diameter) and nuclear (small blue circle; $0''.3$ diameter) MRS spectra discussed in the text. The total spectrum includes the AGN and starburst ring. The nuclear spectrum is dominated by the AGN and is the focus of this paper. A scale bar depicting 100 pc in projection is shown at the lower left.

corrections using prototype pipeline code have been applied to both the stage 2 products and the 1D spectra resulting from stage 3 processing after spectral extraction (see below).

3. Results

We have extracted two spectra from the NGC 7469 MRS data cubes. The first, hereafter the “total” spectrum, is defined as the largest cylindrical aperture that covers the full wavelength extent of MIRI. This aperture has a radius of $1''.8$ centered on the nucleus. The second extraction, meant to isolate the central AGN, is also centered on the nucleus but with a one FWHM diameter ($0''.3$ at $5\ \mu\text{m}$) expanding cone. Because this nuclear aperture is fairly small and dominated by the central AGN by design, a wavelength-dependent aperture correction constructed from standard star observations has been applied to the data before measuring emission line fluxes. Both apertures are drawn on the NIRCcam F150W subarray image in Figure 1.

The two NGC 7469 MIRI spectra are shown in Figure 2, along with the low-resolution Spitzer/IRS spectrum from Stierwalt et al. (2013) for comparison. The Spitzer/IRS spectrum is derived from a single pointing on the nucleus with the short-low ($3''.6$ wide) and long-low ($10''.5$ wide) slits. As in the Spitzer spectrum, the total NGC 7469 MIRI spectrum is dominated by PAH emission features (complexes) at 6.2 , 7.7 , 8.6 , 11.3 , and $12.6\ \mu\text{m}$. There are also weaker PAH features seen at 5.3 , 14.2 , 16.4 , and $17.4\ \mu\text{m}$. Strong, narrow atomic fine-structure emission lines from a variety of species, such as Fe, Ne, Ar, Si, S, O, Mg, and Na, are visible. Emission lines from a number of rotational transitions of warm H_2 are also seen throughout the spectrum. The brightest of these atomic and molecular gas emission lines were visible in the Spitzer

data, but the MIRI spectra reveal many more lines, and the increased resolving power allows for identification of weak features, clear separation of atomic and molecular gas emission lines from nearby PAH features, and the shapes of the mid-infrared lines and hence the dynamics of the atomic and warm molecular gas to be analyzed in detail for the first time. Some residual fringes and low-level continuum variations are also evident in the total and nuclear spectra near, for example, 5 , 13 , and $25\ \mu\text{m}$ in Figure 2. These may be masking additional faint emission features that will require further analysis with improved versions of the pipeline to confidently measure.

Of particular note is that the NGC 7469 nuclear spectrum shows a striking lack of strong PAH emission and an abundance of high-ionization lines tracing the hard ionizing radiation field emerging from the AGN. The ratios of a number of high- to low-ionization features are clearly enhanced in the nuclear spectrum. There are also eight H_2 emission lines present in the nuclear spectrum indicative of warm molecular gas. Finally, there is a slight blue upturn in the nuclear spectrum shortward of about $8\ \mu\text{m}$ that may signal the presence of very warm dust heated by the AGN. The comparison of the two JWST/MIRI spectra demonstrates that in the total spectrum, as in the Spitzer/IRS spectrum, the PAH emission is dominated by the starburst ring, while most of the high-ionization lines (not surprisingly) are coming from the nucleus. The H_2 emission emerges from the ring and the nucleus. The properties of the outflow and the dust and gas in the starburst ring as traced with MIRI are discussed in U et al. (2022) and Lai & Armus (2022), respectively. Here we concentrate on the properties of the high-resolution nuclear spectrum and what they reveal about the AGN and the wind.

3.1. Ionized Gas

We detect emission lines from the nucleus of NGC 7469 spanning a wide range of ionization states, from $[\text{Fe II}]$ with $\text{IP} = 7.9\ \text{eV}$ to $[\text{Mg VII}]$ with $\text{IP} = 186.5\ \text{eV}$, allowing us to explore the properties of the circumnuclear atomic gas as a function of ionization. The coronal lines are very strong in the nucleus of NGC 7469. The $[\text{Ne V}] 14\ \mu\text{m}/[\text{Ne II}]$ and $[\text{O IV}]/[\text{Ne II}]$ line flux ratios are 1.5 and 5.0, respectively, comparable to some of the highest values seen in nearby AGN and AGN-dominated LIRGs with ISO and Spitzer (Genzel et al. 1998; Lutz et al. 2000; Sturm et al. 2002; Armus et al. 2007; Tommasin et al. 2010). In some cases, low-ionization emission features are weak or absent from the nuclear spectrum. An example of this is the $[\text{Fe II}]$ line at $26\ \mu\text{m}$. This line is relatively strong in the Spitzer long-high spectrum (Inami et al. 2013), visible but weak in the total MRS spectrum, and not detected in the nuclear MRS spectrum. This likely indicates that most of the flux detected with Spitzer arises on large physical scales, since the projected size of the long-high slit is significantly larger than the extraction region of the total MRS spectrum.

Because of the high spectral resolving power of MIRI, nearly all of the emission lines are resolved in the MRS nuclear spectrum. All lines show a strong narrow component that dominates the emission, while some show a more complex line profile. The narrow line widths, corrected for instrumental broadening, range from ~ 100 to $400\ \text{km s}^{-1}$, with a median width of about $260\ \text{km s}^{-1}$. While the wavelength calibration is still being refined for MRS and some of the lines have centroids that are clearly offset from their expected positions (e.g., the

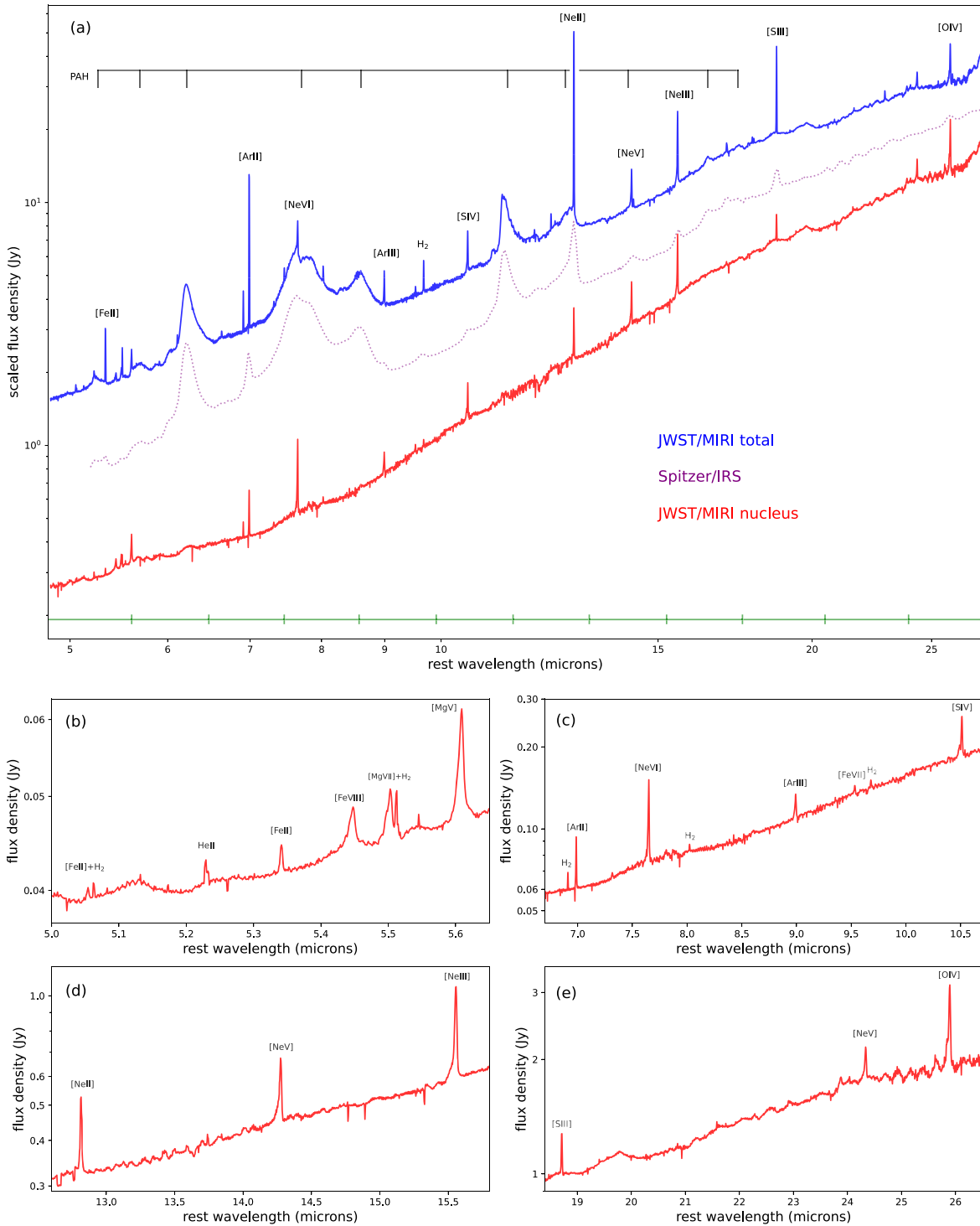


Figure 2. JWST/MIRI mid-infrared spectra of NGC 7469. The top panel (a) is a comparison of the total MIRI/MRS spectrum (blue solid) and the nuclear extraction (red solid) to the Spitzer/IRS low-resolution spectrum (purple dotted) from Stierwalt et al. (2013). All spectra are arbitrarily scaled and presented in the rest frame. Prominent emission lines and PAH features are labeled at the top. Atomic lines covering a wide range of ionization potentials and a number of H₂ lines from warm molecular gas are present in the NGC 7469 nuclear spectrum. The PAH features that dominate the total JWST and Spitzer spectra are very weak in the nuclear spectrum, and the high-ionization lines are significantly enhanced relative to the low-ionization lines. The green line at the bottom of the panel indicates the wavelength ranges of individual MIRI/MRS channels. The bottom four panels (b)–(e) highlight four spectral regions of the nuclear spectrum with individual bright emission features labeled. Asymmetric blue wings and broad profiles are evident on many of the high-ionization emission lines, indicative of fast-moving gas associated with a nuclear outflow.

narrow component of the [Ne V] 14 μ m line is blueshifted from its expected position by $\sim 0.05 \mu$ m), in many cases (e.g., the narrow component of [O IV]), the centroids of the narrow-line components are consistent with systemic velocity. The

wavelength offsets are channel-dependent, and in the current paper, we refrain from comparing the absolute velocities of lines between channels or to other measurements in the literature.

A large number of the emission line profiles exhibit broad blue wings. This broad emission is prominent in the high-ionization coronal lines (e.g., [Ne V], [Ne VI], and [Mg VII]) but absent from the low-ionization lines (e.g., [Ne II]). The high-velocity emission extends up to 1700 km s^{-1} blueward of the narrow component. There is little or no redshifted emission in the high-ionization lines, with the exception of [Mg V] $5.61 \mu\text{m}$ and [Fe VIII] $5.447 \mu\text{m}$, which do show red wings extending out to about 1000 km s^{-1} . We have fit all lines that show broad emission with a simple two-component Gaussian model profile to estimate the basic line parameters. In all cases, we have fit a local, linear continuum under each line that extends from about ± 0.1 to $0.3 \mu\text{m}$ to mitigate against residual low-level continuum variations. The broad components have FWHMs that range from ~ 500 to 1000 km s^{-1} . While we designate these features as broad to facilitate a comparison to the narrow emission, they are far narrower than those from the canonical broad-line region. The FWHM of the $H\beta$ broad line in NGC 7469 is over 4300 km s^{-1} (Peterson et al. 2004). The offsets between the centroids of the narrow and broad components range from ~ 100 to 600 km s^{-1} . The fluxes and widths of the narrow and broad components are presented in Table 1, and a subset of the lines are shown scaled and shifted to a common velocity in Figure 3. Because the line is very bright, the broad blueshifted emission in the [O IV] line was also seen in the Spitzer/IRS long-high spectrum of NGC 7469 (Inami et al. 2013), even though the spectral resolving power was only about 550 and the slit was extremely wide (including emission from the disk and starburst ring). The [Ne III] and [Ne V] $14 \mu\text{m}$ lines were also resolved in the Spitzer spectra, with intrinsic widths of ~ 420 and $\sim 350 \text{ km s}^{-1}$, respectively. The centroid of the [Ne V] line was also blueshifted by about 300 km s^{-1} . Now that the true line profiles are resolved with JWST, the blueshifts seen in the Spitzer data can be understood as the combined effects of a strong narrow feature near systemic and a broad blue wing.

3.2. Warm Molecular Gas

The MIRI MRS spectrum of the nucleus of NGC 7469 reveals the presence of a number of pure rotational emission lines of H_2 that trace the warm molecular gas in the vicinity of the AGN. Eight transitions are detected in the spectrum, with fluxes ranging from ~ 0.5 to $5 \times 10^{-18} \text{ W m}^{-2}$. All of the H_2 lines are resolved, with intrinsic line widths (FWHM) ranging from 124 to 331 km s^{-1} —comparable to or less than those of the low-ionization atomic lines. The $17.05 \mu\text{m}$ S(1) line is the broadest, but its width is highly uncertain. The median line width is $\sim 210 \text{ km s}^{-1}$ FWHM. None of the H_2 emission lines show the broad, blueshifted wings seen on the high-ionization atomic emission lines (see Figure 3).

Following Togi & Smith (2016), we have fit the H_2 line fluxes with a power-law, temperature-dependent excitation function to estimate the characteristic gas temperature and implied mass. The power-law index is 4.55 , and there is approximately $1.3 \times 10^5 M_\odot$ of warm gas at $T \geq 200 \text{ K}$ and an extrapolated mass (down to 50 K) of $\sim 1.2 \times 10^7 M_\odot$ in a $0''.3$ diameter aperture. The latter is approximately 0.4% of the total estimated H_2 mass within a radius of $2''.5$ in NGC 7469 (Davies et al. 2004; Izumi et al. 2020) and 18% of the estimated H_2 mass within a radius of $0''.2$ (Izumi et al. 2020). The measured S(1)/S(2) line flux ratio is similar to the average value

Table 1
Measured Spectral Features

Feature ID	λ_{rest} (μm)	IP (eV)	Flux ($10^{-18} \text{ W m}^{-2}$)	FWHM (km s^{-1})
1	2	3	4	5
$\text{H}_2\text{S}(8)$	5.053		0.64 (0.17)	268 (47)
[Fe II]	5.062	7.9	0.38 (0.07)	<100
He II	5.228	24.6	1.29 (0.19)	298 (33)
[Fe II]	5.340	7.9	1.31 (0.07)	234 (11)
[Fe VIII]	5.447	124	1.98 (0.28)	372 (26)
			4.09 (0.36)	1095 (63)
[Mg VII]	5.503	186.5	1.03 (0.32)	189 (32)
			4.05 (0.42)	621 (36)
$\text{H}_2 \text{ S}(7)$	5.511		1.45 (0.15)	124 (18)
[Mg V]	5.610	109.2	3.51 (0.33)	231 (11)
			9.66 (0.41)	726 (22)
$\text{H}_2\text{S}(6)$	6.11		0.53 (0.05)	175 (12)
6.2 PAH	6.22		27.1 (2.5)	...
$\text{H}_2\text{S}(5)$	6.910		3.05 (0.11)	188 (5)
[Ar II]	6.985	15.8	13.48 (0.61)	261 (10)
[Na III]	7.318	47.3	1.76 (0.25)	427 (29)
[Ne VI]	7.652	126.2	26.7 (1.99)	309 (13)
			18.0 (2.25)	962 (64)
$\text{H}_2\text{S}(4)$	8.025		1.59 (0.23)	214 (23)
[Ar III]	8.991	27.6	7.00 (2.78)	291 (38)
			5.31 (1.47)	563 (156)
[Fe VII]	9.527	99.1	2.07 (0.69)	237 (34)
			2.35 (0.74)	631 (197)
$\text{H}_2\text{S}(3)$	9.665		2.94 (0.63)	265(43)
[S IV]	10.511	34.8	22.86 (0.99)	299 (9)
			10.9 (1.40)	667 (65)
$\text{H}_2\text{S}(2)$	12.279		2.71 (0.51)	202 (29)
[Ne II]	12.814	21.6	49.62 (3.62)	313 (14)
[Ne V]	14.322	97.1	41.77 (3.64)	259 (13)
			32.68 (4.51)	814 (62)
[Ne III]	15.555	41.0	91.61 (4.65)	287 (8)
			45.85 (4.79)	920 (38)
$\text{H}_2\text{S}(1)$	17.035		4.16 (1.95)	331 (140)
[Fe II]	17.936	7.9	2.46 (0.97)	319 (90)
[S III]	18.713	23.3	46.77 (1.37)	207 (5)
[Ne V]	24.318	97.1	42.48 (4.07)	224 (12)
			34.82 (6.24)	861 (85)
[O IV]	25.890	54.9	151.73 (26.31)	261 (20)
			96.4 (34.61)	706 (165)

Notes. Basic properties of the emission lines measured in the JWST/MIRI MRS nuclear spectrum of NGC 7469. Column (1): feature ID; column (2): rest wavelength (μm); column (3): line flux ($10^{-18} \text{ W m}^{-2}$); column (4): intrinsic FWHM (km s^{-1}) after subtraction of the instrumental broadening. Lines that have been fit with an additional broad component have a second entry row. The 1σ uncertainties in the fitted quantities are given in parentheses. The $6.2 \mu\text{m}$ emission feature is a series of resolved components, not a single emission line, so it does not have an entry in column (4).

measured by Tommasin et al. (2010) in a sample of Seyfert galaxies with Spitzer.

3.3. Dust

The strong PAH features that dominate the total mid-infrared spectrum of NGC 7469 are weak or absent from the nuclear spectrum (see Figure 2). The spectrum does have some residual continuum noise that makes identification of very weak and broad PAH features difficult, but it is clear that the strong PAH emission seen in the total MIRI and Spitzer spectra is not present in the nuclear spectrum. This is consistent with the

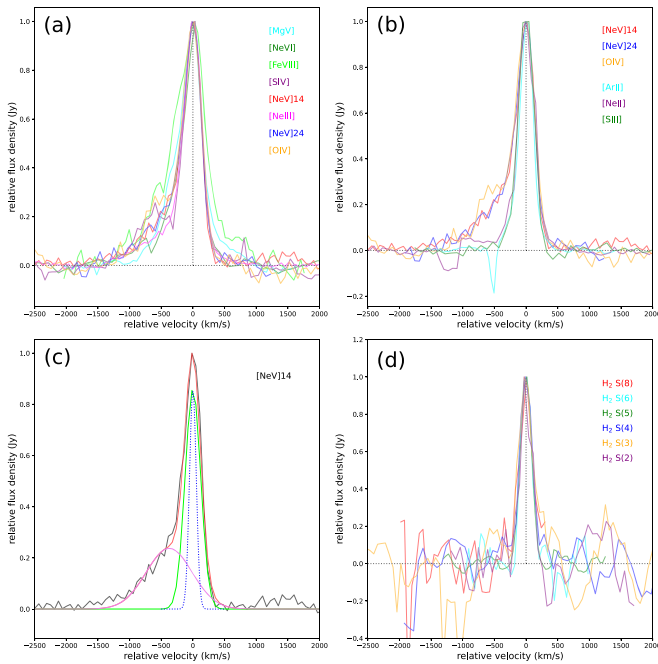


Figure 3. Atomic and H₂ line profiles in the MIRI/MRS nuclear spectrum of NGC 7469. High-ionization lines are shown in panel (a). A comparison of some of the brighter high- and low-ionization lines is shown in panel (b). All lines are continuum-subtracted and have been normalized and shifted to the centroid of the narrow-line peak. Black dotted lines indicate the base level and zero velocity in each case. The high-ionization lines are all asymmetric, with wings that extend up to 1700 km s⁻¹ to the blue. The high-velocity blue wings are not present in the low-ionization lines. A simple two-component Gaussian fit to the 14.3 μm [Ne V] line is shown in panel (c). In this panel, the narrow [Ne V] component is in green, the broad blueshifted component is in violet, and the sum is in red. Also shown, with a blue dotted line, is a Gaussian having a width corresponding to an unresolved line at this wavelength. A number of the H₂ emission lines detected in the NGC 7469 nuclear spectrum are shown in panel (d) for comparison. While the H₂ lines are resolved, they are all symmetric and narrow.

results of Lai & Armus (2022) and Honig et al. (2010). We do, however, detect a weak PAH feature at 6.2 μm with a flux of $\sim 2.7 \pm 0.2 \times 10^{-17}$ W m⁻² and 2.5σ upper limits on the fluxes of the 7.7 and 11.3 μm PAH features of $\leq 9.2 \times 10^{-17}$ and $\leq 3.5 \times 10^{-17}$ W m⁻², respectively. The 6.2 μm nuclear flux is about 0.5% of the PAH emission in the “total” MIRI spectrum. Our 6.2/7.7 PAH flux ratio limit of ≥ 0.11 does not allow us to confidently constrain the grain size, but the 6.2 μm PAH equivalent width (EQW) of 0.07 μm is within the range seen for other AGN (e.g., Spoon et al. 2007).

The NGC 7469 nuclear spectrum is steeply rising over much of the MIRI wavelength range with a slight inflection around ~ 8 μm that may signal the presence of warm dust heated by the AGN. The 15-to-5 μm flux density ratio is ~ 12.5 . There is no indication of either strong silicate absorption or emission at 9.7 or 18 μm. The 9.7 μm silicate strength, as defined in Hao et al. (2007), is 0.02. This is smaller than found for many nearby QSOs, where silicate emission is common, and larger than most Seyfert 2s and ULIRGs, where absorption dominates and the silicate strengths are negative but consistent with other Seyfert 1 galaxies observed with Spitzer (Hao et al. 2005, 2007; Schweitzer et al. 2006; Netzer et al. 2007). For comparison, the silicate strength measured in the Spitzer spectrum of NGC 7469 is -0.14 , indicative of a small apparent absorption, undoubtedly the result of a significant amount of optically thick dust from the starburst ring within the large Spitzer slit. The silicate

strength, together with the 6.2 μm PAH EQW, places NGC 7469 between class 1A and 1B objects in the diagnostic diagram of Spoon et al. (2007). The low silicate strength, weak PAH EQW, and steep spectral slope may also indicate a contribution from ongoing star formation to the nuclear spectrum (Marshall et al. 2018).

4. Discussion

The high spectral resolution of the MIRI MRS data, together with the range of detected atomic and H₂ lines, allows us to probe the dynamics and ionization structure of the atomic gas and the warm molecular gas in NGC 7469 on scales of ~ 100 pc in the mid-infrared for the first time.

It is known that NGC 7469 has an outflowing, highly ionized nuclear wind seen in the near-infrared [Si VI] coronal line on subarcsecond scales (Muller-Sanchez et al. 2011). The atomic gas measured with MIRI is most likely associated with this outflow. One striking difference, however, is that the MIRI data show gas moving at much higher velocity than mapped in [Si VI], which reaches velocities of ± 120 km s⁻¹ at radii of about $0''.2$ – $0''.3$. Broad blueshifted emission extending to nearly ~ 1000 km s⁻¹ is seen in the central spaxel of the Keck/OSIRIS data, but the single Gaussian fits used to construct the outflow model are clearly dominated by slower-moving gas at radii of ~ 60 pc. The high-ionization, high-velocity gas in the JWST MIRI spectrum is also seen as a faint eastern extension in the [Mg V] map produced by U et al. (2022).

The fact that the high-velocity gas is most prominent in the coronal lines is consistent with an ionized, decelerating wind. In this picture, the more highly ionized gas is closer to the AGN and moving at greater speeds. The enhanced blueshifted emission is a result of geometry and possibly extinction, with the receding gas being partially blocked by dust in the inner disk. Despite the high velocities, the bulk of the gas appears to be photoionized, as the [S IV]/[Ne II], the [Ne III]/[Ne II], and the limit on the [Fe II]/[O IV] ratios all imply that shock heating is negligible (Inami et al. 2013). It is likely that the coronal line gas we see in NGC 7469 may also be related to the high-velocity, warm absorber, and emission line gas inferred to exist on much smaller scales (0.1–3 pc) by Grafton-Waters et al. (2020) through modeling of the XMM/RGS spectrum. Blueshifted coronal lines in the mid-infrared have been seen in nearby ULIRGs with powerful outflows (e.g., Spoon & Holt 2009), and it is reminiscent of the kinematic structures seen in some narrow-line Seyfert type 1 galaxies known as “blue outliers” (Komossa et al. 2008), typically identified via asymmetric optical [O III] emission.

To better understand the NGC 7469 outflow probed with MIRI, we plot the broad line widths and broad-to-narrow line flux ratios as a function of ionization potential and critical density in Figure 4. With the exception of the [Mg VII] line at 5.503 μm, which is partially blended with H₂S(7), the broad line widths show a moderate correlation with ionization potential and the broad-to-narrow line flux ratio (Pearson’s $r = 0.58$ and 0.57 , respectively). There is no correlation with critical density, but this is not surprising, since the ratio of the [Ne V] 14 and 24 μm lines is ~ 0.96 (~ 0.94 for the broad lines alone), indicating that the coronal line gas is nearly in the low-density limit with $n_e < 1000$ cm⁻³ (see Alexander et al. 1999). The primary correlations of the line widths and relative fluxes are with ionization, similar to what is seen in NGC 1068 (Lutz

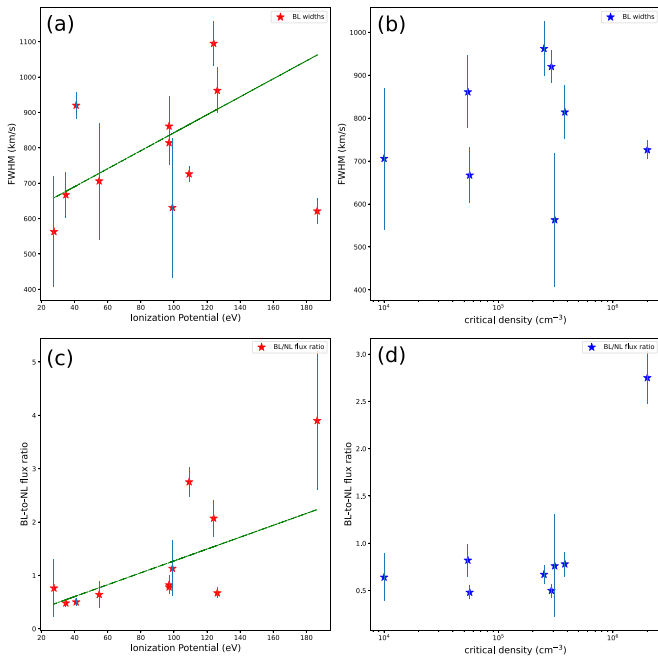


Figure 4. Emission line properties as a function of ionization and critical density in NGC 7469. The broad line widths and broad-to-narrow component flux ratios are plotted as a function of ionization potential (panels (a) and (c)) and critical density (panels (b) and (d)) for the fine-structure lines in the nuclear spectrum of NGC 7469. The lines show a correlation of broad line width and broad-to-narrow line flux ratio with ionization potential. Linear fits are shown as green dashed lines in panels (a) and (c), excluding the [Mg VII] $5.5 \mu\text{m}$ line, which is blended with H_2 .

et al. 2000). The correlations among fit components strengthen the picture of the simple model that is evident from the line profiles alone, namely, that the prominence of the high-velocity, mostly blueshifted gas among the coronal lines seen with MIRI suggests a decelerating, stratified, AGN-driven outflow in NGC 7469.

To estimate the mass outflow rate in the coronal gas, we need to know the gas density, filling factor, maximum velocity, and lateral surface area of the wind. From the [Si VI] emission line map, Muller-Sanchez et al. (2011) estimated a mass outflow rate of $\sim 4 M_{\odot} \text{yr}^{-1}$, assuming a density of 5000cm^{-3} , filling factor of 0.001, wind lateral surface area of $11 \times 10^4 \text{pc}^2$, and maximum velocity of 130km s^{-1} (see their Equation 1). If the high-velocity gas we see with JWST emerges in the wind over an area consistent with our aperture and the eastern extension in U et al. (2022), and the gas has a maximum velocity of 1700km s^{-1} , density of $\sim 500 \text{cm}^{-3}$, and filling factor of 0.001, then we would arrive at a mass outflow rate of $\sim 0.5\text{--}1 M_{\odot} \text{yr}^{-1}$. If the gas filling factor is larger, more typical of an AGN narrow-line region (e.g., Storchi-Bergmann et al. 2010), then the outflow rate could be up to $\sim 5 M_{\odot} \text{yr}^{-1}$, close to the value estimated by Muller-Sanchez et al. (2011). The mass outflow rate is highly uncertain but still much larger than the gas accretion rate required to power the AGN. Using the scaling between [O IV] and the black hole accretion rate (BHAR) in Stone et al. (2022), we estimate a BHAR of $\sim 4.1 \times 10^{-2} M_{\odot} \text{yr}^{-1}$, or roughly 1–2 orders of magnitude less than the mass outflow rate in the ionized wind.

As has been shown by Komossa & Xu (2007), the narrow line widths can be used as a surrogate for the stellar velocity dispersion and therefore used to estimate the black hole mass in Seyfert galaxies, once components associated with any

outflowing gas are removed. While the high-ionization lines show blueshifted emission in the MIRI MRS spectrum of NGC 7469, many of the narrow components have centroids consistent with the systemic velocity. This strong narrow-line component can be used to estimate the mass of the central SMBH, assuming it dominates the dynamical mass in the sampled volume.

Correlations between the widths and luminosities of the mid-infrared [Ne V] $14.3 \mu\text{m}$ and [O IV] $25.9 \mu\text{m}$ lines and the mass of the central SMBH were established by Dasyra et al. (2008) using Spitzer/IRS data of a sample nearby Seyfert galaxies, including NGC 7469. Using the width of the narrow component of the [Ne V] and [O IV] lines in the MIRI/MRS nuclear spectrum, we estimate a mass of $\sim 6 \times 10^6 M_{\odot}$, about half the value calculated from reverberation line estimates (Peterson et al. 2004) or one-third the value estimated by Nguyen et al. (2021) from fits to the rotating central nuclear disk measured in [C I] and CO with ALMA. We assume here that the shift seen in the [Ne V] $14.3 \mu\text{m}$ line is due to the wavelength calibration, as described in Section 3.1. Similarly, the luminosities of the narrow lines imply SMBH masses of 4.4 and $4.8 \times 10^7 M_{\odot}$ for [Ne V] and [O IV], respectively, or about a factor of 4–5 larger than the reverberation line estimate. As noted by Dasyra et al. (2008), a large Eddington ratio would lower the SMBH mass predicted from the [O IV] and [Ne V] line luminosities, perhaps bringing them more in line with the reverberation line estimate. By contrast, the widths of the broad components in the MIRI/MRS nuclear spectrum imply SMBH masses that are a factor of 75–80 higher than measured by Peterson et al. (2004). This is consistent with our association of the high-velocity gas with the outflow. Future studies of larger samples of nearby Seyfert galaxies with JWST, where outflowing and infalling gas can be identified and separated with the MIRI and NIRSpc IFUs both spatially and spectrally, could provide a revised calibration of this correlation and a powerful tool to estimate SMBH masses in Seyfert galaxies.

The strong but relatively narrow H_2 lines in the nuclear spectrum, along with the relatively flat power-law index, suggest that warm molecular gas in the central $\sim 100 \text{pc}$ is dominated by AGN heating. This is consistent with the relative dip in the line dispersion seen by U et al. (2022) on the nucleus. The fan-shaped structure to the northwest seen as an enhancement in the H_2 dispersion by U et al. (2022) may reveal a molecular gas shock heated by the wind. The enhanced central [C I] emission has also been suggested as evidence for AGN heating of the circumnuclear gas in an X-ray Dissociation Region (XDR) (Izumi et al. 2020). The near-infrared H_2 line ratios can be explained by AGN heating or arise in dense gas illuminated by hot stars (Davies et al. 2005). If the $6.2 \mu\text{m}$ PAH emission seen in the nuclear spectrum is powered by star formation, then the implied star formation rate is $\sim 0.4 M_{\odot} \text{yr}^{-1}$ (Pope et al. 2008), or less than 1% of the total star formation rate in NGC 7469.

5. Summary

We provide an analysis of the high-resolution, mid-infrared spectrum of the nucleus of NGC 7469 taken with the MIRI instrument on board the JWST. The rich set of emission features has provided a detailed picture of the dynamics and physical conditions of the ionized atomic and warm molecular gas and the dust in the inner $\sim 100 \text{pc}$ of NGC 7469. Our results can be briefly summarized as follows.

1. There are 19 identified emission lines covering a wide range of ionization potential up to 187 eV. The high-ionization lines all show broad, blueshifted emission reaching up to -1700 km s^{-1} with respect to bright, narrow systemic emission. The broad, blueshifted emission is not seen in the low-ionization lines. The width of the broad emission and the broad-to-narrow line flux ratios correlate with ionization potential. We interpret the results as indicative of a decelerating, stratified, AGN-driven outflow emerging from the NGC 7469 nucleus. The estimated mass outflow rate in the wind, $\sim 1\text{--}5 M_{\odot} \text{ yr}^{-1}$, is significantly larger than the current black hole accretion rate needed to power the AGN.
2. There are eight pure rotational H_2 emission lines detected in the nuclear spectrum. The H_2 lines have a median intrinsic FWHM $\sim 210 \text{ km s}^{-1}$, with none showing the broad, blueshifted emission seen in the high-ionization atomic lines. We estimate that there is a total mass of warm gas of $\sim 1.2 \times 10^7 M_{\odot}$ in the central 100 pc. The high temperature and relatively narrow H_2 lines in the nuclear spectrum suggest that this warm molecular gas is heated by the AGN.
3. The PAH features that dominate the total mid-infrared spectrum of NGC 7469 are significantly weaker in the nuclear spectrum. We detect a $6.2 \mu\text{m}$ feature with an EQW $\sim 0.07 \mu\text{m}$ and a flux of $2.7 \times 10^{-17} \text{ W m}^{-2}$. If the PAH emission in the nuclear spectrum is a result of star formation, then the implied star formation rate is $\sim 0.4 M_{\odot} \text{ yr}^{-1}$, or less than 1% of the total star formation rate in NGC 7469.
4. The NGC 7469 nuclear spectrum is steeply rising over the MIRI wavelength range. There is no indication of strong silicate absorption or emission at $9.7 \mu\text{m}$. The measured silicate strength is 0.02, significantly smaller than found for many nearby QSOs but consistent with other Seyfert 1s.

The mid-infrared nuclear spectrum of NGC 7469 presented here demonstrates the power of MIRI/MRS to disentangle the complex excitation and kinematic properties in the circum-nuclear environments of nearby merging galaxies that are both feeding AGN and rapidly producing stars. These regions are inherently multiphase, and the ability to spatially and spectrally resolve the atomic and molecular gas emission, as well as the dust in these galaxies, is a unique ability made possible with infrared integral field spectrographs on JWST. Planned and future JWST observations of NGC 7469 and other nearby LIRGs and Seyfert galaxies will undoubtedly shed even more light on feeding and feedback at the centers of rapidly evolving galaxies.







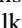





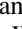
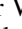
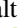




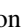


This work is based on observations made with the NASA/ESA/CSA JWST. The research was supported by NASA grant JWST-ERS-01328. The data were obtained from the Mikulski Archive for Space Telescopes at the Space Telescope Science Institute, which is operated by the Association of Universities for Research in Astronomy, Inc., under NASA contract NAS 5-03127 for JWST. The observations can be accessed via <https://doi.org/10.17909/0fe2-cf33>. V.U. acknowledges funding support from NASA Astrophysics Data Analysis Program (ADAP) grant 80NSSC20K0450. The Flatiron Institute is supported by the Simons Foundation. A.M.M. acknowledges support from the National Science Foundation







under grant No. 2009416. A.S.E. and S.L. acknowledge support from NASA grant HST-GO15472. H.I. and T.B. acknowledge support from JSPS KAKENHI grant No. JP21H01129 and the Ito Foundation for Promotion of Science. Y.S. was funded in part by the NSF through the Grote Reber Fellowship Program administered by Associated Universities, Inc./National Radio Astronomy Observatory. F.M.-S. acknowledges support from NASA through ADAP award 80NSSC19K1096. S.A. gratefully acknowledges support from ERC Advanced grant 789410, the Swedish Research Council, and the Knut and Alice Wallenberg (KAW) Foundation. K.I. acknowledges support by the Spanish MCIN under grant PID2019-105510GB-C33/AEI/10.13039/501100011033. This work was also partly supported by the Spanish program Unidad de Excelencia María de Maeztu CEX2020-001058-M, financed by MCIN/AEI/10.13039/501100011033. This research has made use of the NASA/IPAC Extragalactic Database (NED), which is operated by the Jet Propulsion Laboratory, California Institute of Technology, under contract with the National Aeronautics and Space Administration. The National Radio Astronomy Observatory is a facility of the National Science Foundation operated under cooperative agreement by Associated Universities, Inc. The authors would also like to thank an anonymous referee whose comments improved the quality and clarity of this paper.

Facility: JWST (NIRCam and MIRI).

Software: astropy (Astropy Collaboration et al. 2013, 2018), Cosmology calculator (Wright 2006), JWST Science Calibration Pipeline (Bushouse et al. 2022), CAFE (Marshall et al. 2007, T. Díaz-Santos et al. 2022, in preparation), JDAVis (Lim et al. 2022), lmfit (Newville et al. 2014), Matplotlib (Hunter 2007), Numpy (Van der Walt et al. 2011), QFitsView (Ott 2012), SciPy (Virtanen et al. 2020).

ORCID iDs

- L. Armus  <https://orcid.org/0000-0003-3498-2973>
 T. Lai  <https://orcid.org/0000-0001-8490-6632>
 V. U  <https://orcid.org/0000-0002-1912-0024>
 K. L. Larson  <https://orcid.org/0000-0003-3917-6460>
 T. Díaz-Santos  <https://orcid.org/0000-0003-0699-6083>
 A. S. Evans  <https://orcid.org/0000-0003-2638-1334>
 M. A. Malkan  <https://orcid.org/0000-0001-6919-1237>
 J. Rich  <https://orcid.org/0000-0002-5807-5078>
 A. M. Medling  <https://orcid.org/0000-0001-7421-2944>
 D. R. Law  <https://orcid.org/0000-0002-9402-186X>
 H. Inami  <https://orcid.org/0000-0003-4268-0393>
 F. Muller-Sanchez  <https://orcid.org/0000-0002-2713-0628>
 V. Charmandaris  <https://orcid.org/0000-0002-2688-1956>
 P. van der Werf  <https://orcid.org/0000-0001-5434-5942>
 S. Stierwalt  <https://orcid.org/0000-0002-2596-8531>
 S. Linden  <https://orcid.org/0000-0002-1000-6081>
 G. C. Privon  <https://orcid.org/0000-0003-3474-1125>
 L. Barcos-Muñoz  <https://orcid.org/0000-0003-0057-8892>
 C. Hayward  <https://orcid.org/0000-0003-4073-3236>
 Y. Song  <https://orcid.org/0000-0002-3139-3041>
 P. Appleton  <https://orcid.org/0000-0002-7607-8766>
 S. Aalto  <https://orcid.org/0000-0002-5828-7660>
 T. Bohn  <https://orcid.org/0000-0002-4375-254X>
 T. Böker  <https://orcid.org/0000-0002-5666-7782>
 M. J. I. Brown  <https://orcid.org/0000-0002-1207-9137>
 L. Finnerty  <https://orcid.org/0000-0002-1392-0768>
 J. Howell  <https://orcid.org/0000-0001-6028-8059>

K. Iwasawa  <https://orcid.org/0000-0002-4923-3281>
 F. Kemper  <https://orcid.org/0000-0003-2743-8240>
 J. Marshall  <https://orcid.org/0000-0001-7712-8465>
 J. M. Mazzarella  <https://orcid.org/0000-0002-8204-8619>
 J. McKinney  <https://orcid.org/0000-0002-6149-8178>
 E. J. Murphy  <https://orcid.org/0000-0001-7089-7325>
 D. Sanders  <https://orcid.org/0000-0002-1233-9998>
 J. Surace  <https://orcid.org/0000-0001-7291-0087>

References

- Alexander, T., Sturm, E., Lutz, D., et al. 1999, *ApJ*, 512, 204
 Arav, N., Xu, X., Kriss, G. A., et al. 2020, *A&A*, 633, A61
 Armus, L., Charmandaris, V., & Soifer, B. T. 2020, *NatAs*, 4, 467
 Armus, L., Charmandaris, V., Bernard-Salas, J., et al. 2007, *ApJ*, 656, 148
 Armus, L., Mazzarella, J. M., Evans, A. S., et al. 2009, *PASP*, 121, 559
 Astropy Collaboration, Robitaille, T. P., Tollerud, E. J., et al. 2013, *A&A*, 558, A33
 Astropy Collaboration, Price-Whelan, A. M., Sipocz, B. M., et al. 2018, *AJ*, 156, 123
 Bohn, T., Inami, H., Diaz-Santos, T., et al. 2022, *ApJL*, 941, L36
 Bushouse, H., Eisenhamer, J., Dencheva, N., et al. 2022, *spacetelescope/jwst: JWST v1.6.2*, Zenodo, doi:10.5281/zenodo.6984366
 Dasyra, K. M., Ho, L. C., Armus, L., et al. 2008, *ApJL*, 674, L9
 Davies, R. I., Sternberg, A., Lehnert, M. D., & Tacconi-Garman, L. E. 2005, *ApJ*, 633, 105
 Davies, R. I., Tacconi, L. J., & Genzel, R. 2004, *ApJ*, 602, 148
 Díaz-Santos, T., Alonso-Herrero, A., Colina, L., Ryder, S. D., & Knapen, J. H. 2007, *ApJ*, 661, 149
 Genzel, R., Lutz, D., Sturm, E., et al. 1998, *ApJ*, 498, 579
 Grafton-Waters, S., Branduardi-Raymont, G., Mehdipour, M., et al. 2020, *A&A*, 633, A62
 Hao, L., Weedman, D. W., Spoon, H. W. W., et al. 2007, *ApJL*, 655, L77
 Hao, L., Spoon, H. W. W., Sloan, G. C., et al. 2005, *ApJL*, 625, L75
 Honig, S. F., Kishimoto, M., Gandhi, P., et al. 2010, *A&A*, 515, A23
 Houck, J. R., Roellig, T. L., van Cleve, J., et al. 2004, *ApJS*, 154, 18
 Hunter, J. D. 2007, *CSE*, 9, 90
 Inami, H., Armus, L., Charmandaris, V., et al. 2013, *ApJ*, 777, 156
 Izumi, T., Nguyen, D. D., Imanishi, M., et al. 2020, *ApJ*, 898, 75
 Kim, D. C., Evans, A. S., Vavilkin, T., et al. 2013, *ApJ*, 768, 102
 Komossa, S., & Xu, D. 2007, *ApJL*, 667, L33
 Komossa, S., Xu, D., Zhou, H., Storchi-Bergmann, T., & Binette, L. 2008, *ApJ*, 680, 926
 Labiano, A., Argyriou, I., Álvarez-Márquez, J., et al. 2021, *A&A*, 656, A57
 Lai, T. S. Y., & Armus, L. 2022, arXiv:2209.06741
 Larson, K. L., Sanders, D. B., Barnes, J. E., et al. 2016, *ApJ*, 825, 128
 Lim, P. L., O'Steen, R., Earl, N., et al. 2022, *spacetelescope/jdaviz: v2.8.0*, Zenodo, doi:10.5281/zenodo.6877878
 Lutz, D., Sturm, E., Genzel, R., et al. 2000, *ApJ*, 536, 697
 Marshall, J. A., Elitzur, M., Armus, L., Diaz-Santos, T., & Charmandaris, V. 2018, *ApJ*, 858, 59
 Marshall, J. A., Herter, T. L., Armus, L., et al. 2007, *ApJ*, 670, 129
 Muller-Sanchez, F., Prieto, M. A., Hicks, E. K. S., et al. 2011, *ApJ*, 739, 69
 Netzer, H., Lutz, D., Schweitzer, M., et al. 2007, *ApJ*, 666, 806
 Newville, M., Stensitzki, T., Allen, D. B., & Ingargiola, A. 2014, *LMFIT: Nonlinear Least-Square Minimization and Curve-Fitting for Python v0.8.0*, Zenodo, doi:10.5281/zenodo.11813
 Nguyen, D. D., Izumi, T., Thater, S., et al. 2021, *MNRAS*, 504, 4123
 Ott, T. 2012, *QFitsView: FITS file viewer*, Astrophysics Source Code Library ascl:1210.019
 Peterson, B. M., Ferrarese, L., Gilbert, K. M., et al. 2004, *ApJ*, 613, 682
 Petric, A. O., Armus, L., Howell, J., et al. 2011, *ApJ*, 730, 28
 Pontoppidan, K., Blome, C., Braun, H., et al. 2022, *ApJ*, 936, L14
 Pope, A., Chary, R.-R., Alexander, D. M., et al. 2008, *ApJ*, 675, 1171
 Rieke, G. H., Wright, G. S., Boker, T., et al. 2015, *PASP*, 127, 584
 Robbleto-Orus, A. C., Torres-Papaqui, J. P., Longinotti, A. L., et al. 2021, *ApJL*, 906, L6
 Sanders, D. B., Mazzarella, J. M., Kim, D. C., Surace, J. A., & Soifer, B. T. 2003, *AJ*, 126, 1607
 Schweitzer, M., Lutz, D., Sturm, E., et al. 2006, *ApJ*, 649, 79
 Spoon, H. W. W., & Holt, J. 2009, *ApJL*, 702, L42
 Spoon, H. W. W., Marshall, J. A., Houck, J. R., et al. 2007, *ApJL*, 654, L49
 Stierwalt, S., Armus, L., Surace, J. A., et al. 2013, *ApJS*, 206, 1
 Stierwalt, S., Armus, L., Charmandaris, V., et al. 2014, *ApJ*, 790, 124
 Stone, M., Pope, A., McKinney, J., et al. 2022, *ApJ*, 934, 27
 Storchi-Bergmann, T., Lopes, R. D. S., McGregor, P. J., et al. 2010, *MNRAS*, 402, 819
 Sturm, E., Lutz, D., Verma, A., et al. 2002, *A&A*, 393, 821
 Togi, A., & Smith, J. D. T. 2016, *ApJ*, 830, 18
 Tommasin, S., Spinoglio, L., Malkan, M. A., & Fazio, G. 2010, *ApJ*, 709, 1257
 U, V., Medling, A. M., Inami, H., et al. 2019, *ApJ*, 871, 166
 U, V., Lai, T., Bianchin, M., et al. 2022, *ApJL*, 940, L5
 Van der Walt, S., Colbert, S. C., & Varoquaux, G. 2011, *CSE*, 13, 22
 Virtanen, P., Gommers, R., Oliphant, T. E., et al. 2020, *NatMe*, 17, 261
 Wright, E. L. 2006, *PASP*, 118, 1711